IEEE Access
Multidisciplinary ⋮ Rapid Review ⋮ Open Access Journal

Received November 19, 2021, accepted November 30, 2021, date of publication December 3, 2021,
date of current version December 10, 2021.

Digital Object Identifier 10.1109/ACCESS.2021.3132393

A Comparative Study of 2D and 3D Digital Image Correlation Approaches for the Characterization and Numerical Analysis of Composite Materials

JAVIER PISONERO[1], JORGE LÓPEZ-REBOLLO[1], ROBERTO GARCÍA-MARTÍN[2], MANUEL RODRÍGUEZ-MARTÍN[2], LUIS JAVIER SÁNCHEZ-APARICIO[3], A. MUÑOZ-NIETO[1], AND DIEGO GONZÁLEZ-AGUILERA[1]

[1]Department of Cartographic and Land Engineering, Higher Polytechnic School of Ávila, University of Salamanca, 05003 Ávila, Spain
[2]Department of Mechanical Engineering, Higher Polytechnic School of Zamora, University of Salamanca, 49022 Zamora, Spain
[3]Department of Construction and Technology in Architecture (DCTA), Universidad Politécnica de Madrid, 28040 Madrid, Spain

Corresponding author: Javier Pisonero (j_pisonero@usal.es)

This work was supported in part by the European Regional Development Fund (ERDF) Funds through the V Sudoe Interreg Program within the framework of the lightER, eco-friendliER and safER COMPosite PRESSure tanks (COMPRESSer) Project under Grant SOE2/P1/E0643, and in part by the Ministry of Science, Innovation and Universities through the Project Fusión de tecnologías no destructivas y métodos de simulación numérica para la inspección y monitorización de uniones en nuevos materiales y en procesos de fabricación aditiva (FaTIMA) under Grant RTI2018-099850-B-I00.

ABSTRACT This article makes a comparison between different Digital Image Correlation methods to determinate the main mechanical characteristics of composite materials. More specifically Carbon Fiber Reinforced Polymers. For this purpose, several tensile tests were carried out using the same camera and lens model. Different statistical methods as well as probabilistic numerical simulations were performed with the aim of evaluating the discrepancies between methods, and between different mechanical parameters. We want to highlight the consistency of the results, enabling the possibility of using 3D methods with non-planar specimen for determining the mechanical properties of Carbon Fiber Reinforced Polymers. In this case, the novelty is focused on the use of different configurations (2D and 3D) to study the differences in terms of results. the objective is not the specific characterization of CFRP, but to analyze the way in which the use of a dataset from DIC3D or, on the contrary, from DIC2D affects the final results. According to this, it is possible to concluded that significative differences arise in the evaluation of the elastic properties that could be assigned to the uncertainties of the methods. However, this significance does not appear in the results of the probabilistic simulation.

INDEX TERMS Carbon fiber reinforced polymer, composite, digital image correlation, finite element method.

I. INTRODUCTION

Composite materials are a real alternative to the traditional steel-based solutions in engineering due to their mechanical properties, environmental resistance (especially in corrosive atmospheres) [1], [2], fatigue performance [3]–[5] and a high weight-resistance ratio [6]. This type of material could be applied to different products such as pressure pipes and vessels [7], [8], most of them made of Carbon Fiber Reinforced Polymer (CFRP) [9], [10] and Glass Fiber Reinforced Polymer (GFRP). From a numerical point of view, composite materials are more complex than metallic materials. This is due to the wide range of uncertainties during manufacturing and the own complexity of materials [11], [12]. Fiber orientation is one of the main factors, generating an intrinsic heterogeneity to the composite [13]–[15]. Due to this variability of performance, the product design is more complicated than other orthotropic materials, requiring the use of advanced numerical simulations able to represent this heterogeneity. In this context the use of probabilistic approaches based on the use of the Finite Element Method (FEM) could be considered as a feasible solution [16]–[18]. These approaches require the proper definition of the mechanical properties of the composite solution through the application of large experimental campaigns that allow to reproduce their probabilistic density functions (PDFs).

The associate editor coordinating the review of this manuscript and approving it for publication was Agustin Leobardo Herrera-May.

Different devices can be used for the direct measurement of the material's properties like Linear Displacement Transducer Design (LVDT) [19], sensors as laser transducers, extensometers or strains gauges, with the same precision as the DIC [20]. But the presence of different factors or alterations in these sensors might entail inaccuracies and erroneous data measurements that could vary the inputs of the PDFs. For more details about the different factors the reader is refereed to García-Martín *et al.* [21].

In order to avoid these limitations, the Scientific Community has developed different non-contact techniques which can evaluate all the strains over the specimen. Among the main techniques available to determinate the global mechanical characteristics are Moiré Interferometry [22]; Particle Image Velocimetry (PIV) [23]; photoelasticity [24]; multi-camera tracking and the Digital Image Correlation (DIC) [25]–[27].

In this context, DIC supposes a good technique for the characterisation of heterogeneous materials such as wood [28], concrete [29] or composites [25], [30]–[32]. There are two types of DIC strategies: the first one consists of a two-dimensional approach (2D DIC), while the second consists of a three-dimensional approach (3D DIC) [6], [31]. While the 2D DIC approach allows the measurement of displacements and strains in a single study plane, the 3D DIC approach allows the measurement of displacements that take place in different directions out of the main plane [33]. The main advantage of the 2D DIC is the possibility to use a simple setup using a single camera and without the need for external calibration, so the processing time is faster. However, the camera must be positioned completely orthogonally to the study plane and the uncertainties that can occur out of plane can be a disadvantage when this technique is applied [31]. For its part, 3D DIC requires a more complex setup using several cameras, which must be synchronised, in order to solve their relative orientation, requiring longer processing times due to its inner calibration and the high number of images acquired. However, in applications where the geometry is non-planar is the unique approach valid for assessing the mechanical characteristics of the material. This issue is especially relevant in composite designs made of CFRP and using filament winding processes, in which the manufacture of flat specimens for mechanical analysis is not common [34]–[36]. In these specimens the stresses are mainly produced in the plane of the shell (thin shell theory) [37], making use of 3D approaches necessary the strains produced. In this context, it is necessary to make a comparison between the 2D and 3D DIC approaches in order to verify the suitability of the 3D method for determining the mechanical properties of non-planar CFRP specimens for numerical simulations. This comparison has to be exhaustive, not only analyzing the results obtained by the simulations or the results of the test. It is necessary to carry on a statistical comparison.

In this case, the novelty is focused on the use of different configurations (2D and 3D) to study the differences in terms of results. The objective is not the specific characterization of the CFRP, but to analyze the way in which the use of a dataset from DIC3D or, on the contrary, from DIC2D affects the results. After this introduction, Section 2 describes the materials and methods used for this study, namely 2D DIC, 3D DIC and probabilistic numerical simulations. In Section 3 the experimental results are outlined. Finally, Section 4 shows the conclusions of the research and future projects.

II. MATERIALS & METHODS

A. COMPOSITE SOLUTION AND SPECIMEN PREPARATION

For this work, the composite solution used was a CFRP manufactured with fiber CC 200 T-120, epoxy resin CR82 and complemented by a hardener Biresin CH80-10. The mechanical properties of the different constituents can be consulted in [21].

The manufacturing process of the specimen has been based on ISO 527:1997 [38], [39]. A total of 25 specimens were done, each one with a total of 9 layers with orthogonal orientation among them. The process of manufacturing was the following one: (i) fiber placement with the corresponding orientation; (ii) resin impregnation; and (iii) pressure application to avoid possible resin defects. After placing all the layers, the entire block was introduced in a drying oven at a temperature of 50 °C during 50 minutes. As a result, a CFRP composite with an average thickness of 2 mm apt to the manufacturing of pressure vessels was obtained. When the composite block was completed, it was cut with a Computer Numerical Control (CNC) machine.

B. TEST SET UP AND SPECIMEN PREPARATION

A Servosis ME-405/50/5 test machine was used for performing the tensile test. This machine provides a maximum load of 500 kN, with a TC50Kn REP transducer as the load cell and MTS Model XSA304A Grips as the used in past works [21]. Added to the test machine, it is necessary to use cameras for performing the DIC tests. Specifically, a total of three DSLR Canon 700D cameras, equipped with a 60 mm macro-lens and a CMOS APS-C sensor of 22.3 $\times$ 14.9 mm, were used for performing the DIC tests. The image size was of 5184 x 3456 px with a pixel size of 4.3 μm. Two cameras were used for 3D DIC and one camera was used for 2D DIC. The 2D DIC camera was placed orthogonal to the plane of the specimen with the aim of minimizing possible uncertainties. The verticality of the specimen has been guaranteed with an inclinometer and with a micrometric ball joint. So, the orthogonality between optic axes of specimen and camera is guaranteed. 3D cameras are placed in both sides and the 2D DIC camera is the one in the middle, orthogonal to the specimen. [40]. Meanwhile, the cameras used for the 3D-DIC were placed forming a stereo angle of 15° (Figure 1) in order to avoid possible depth of field problems [41].

For automating the acquisition process, the cameras were connected to a Programmable Logic Controller (PLC), Siemens Logo. The PLC was programmed to simultaneously send a signal to the cameras and thus capture the

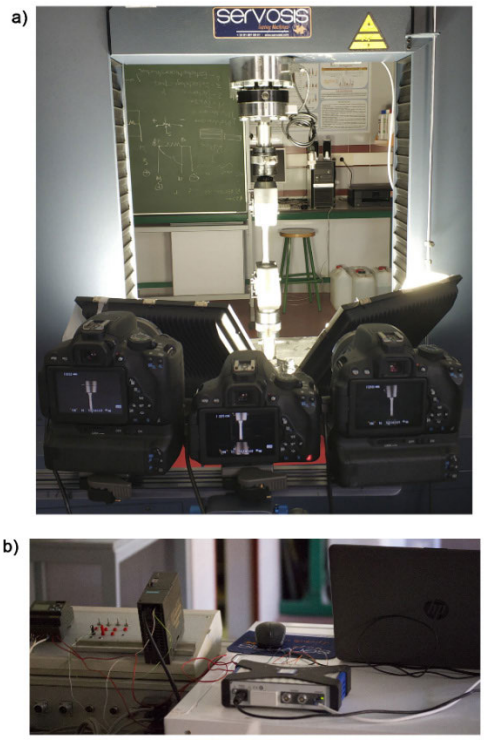

FIGURE 1. General view of the a) image acquisition system and b) data acquisition system. 3D cameras are placed in both sides and the 2D DIC camera is the one in the middle, orthogonal to the specimen.

images. Also, the machine and the PLC were connected to a data acquisition system, QUANTUM, which collects all data. Additionally, two led spotlights were used with the aim of providing a good illumination during the tensile tests (Figure 1).

Finally, the load increment of the test was calculated according with ISO 527-4 [38], [39]. Result to this, the cameras were programmed for capturing one image per second.

For the specimen preparation, first of all is necessary to apply the Speckle pattern. Speckle pattern is one of the most important factors for the final results of the DIC [42]. For this work, a computer speckle pattern was used, since could be considered the most robust and reliable way to create it. To this end, the following considerations were taken into account [43], [46], [46], [47]: i) pattern randomness; ii) circular spots; and iii) covering among 40-70% of the specimen surface, in order to reduce homogeneity. The Mean Intensity Gradient (MIG) was used for assessing the quality of the pattern [48], [49].

Taking into consideration the previous specification, a speckle pattern was designed following the approach proposed by [21]. First of all, a regular mesh with circular specks was created, being the principal parameters for this mesh the diameter, d, of the spots, which is comprised between 3-5 pixels, and the separation (*step*) among centres. The randomness of the pattern was generated applying a Gaussian random factor. The pattern was developed with

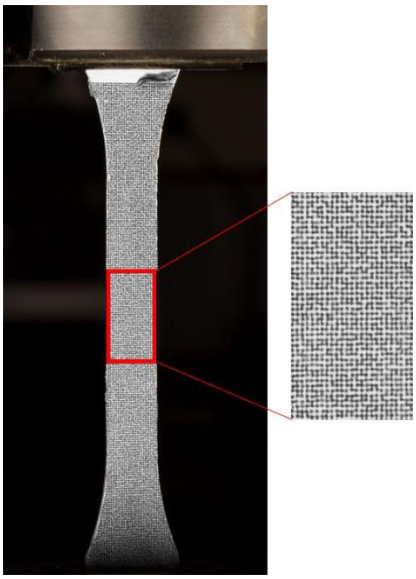

FIGURE 2. Speckle pattern used.

a Matlab©script obtaining a MIG of 56, considering it as acceptable [50]. The defined diameter, d, was 0.324 mm and the step was 0.432 mm. Figure 2 shows the designed speckle impregnate into the specimen.

C. DIGITAL IMAGE CORRELATION APPROACHES

This section describes the different DIC strategies used for estimating the mechanical properties of the composite solution, namely Young Modulus (E), Poisson ratio (v) and Tensile strength (T). To this end, an ad-hoc set-up was designed to compare the two techniques: on the one hand, the 2D DIC method was applied with the images captured by the central camera. Meanwhile, the 3D DIC method was fed with the images captured by the stereo system (Figure 1). After completion of the test and the data acquisition, the mechanical properties have been defined following the workflow showed in Figure 3.

1) 2D DIGITAL IMAGE CORRELATION

The Bundle Adjustment (BA) approach was applied in order to obtain the inner calibration of the camera. This method needs a set of images – about 20 – of a flat checkboard calibration target, with variations of position and orientation. The BA algorithm allows to minimise the overall re-projection error of the corners of squares (control points) extracted from the checkerboard calibration target. Then, a Gaussian radial distortion model is applied in order to compensate the distortion of the lens (Eq. 1).

$$\begin{bmatrix} x_d \\ y_d \end{bmatrix} = \left(1 + k_1 r^2 + k_2 r^4 + k_3 r^6\right) \cdot \begin{bmatrix} x \\ y \end{bmatrix} + \begin{bmatrix} 2p_1 xy + p_2\left(r^2 + 2x^2\right) \\ p_1\left(r^2 + 2y^2\right) + 2p_2 xy \end{bmatrix} \quad (1)$$

where $r^2 = x^2 + y^2$ and represents the radial distance, r, computed from the images' coordinates (x,y); (x_d, y_d) are

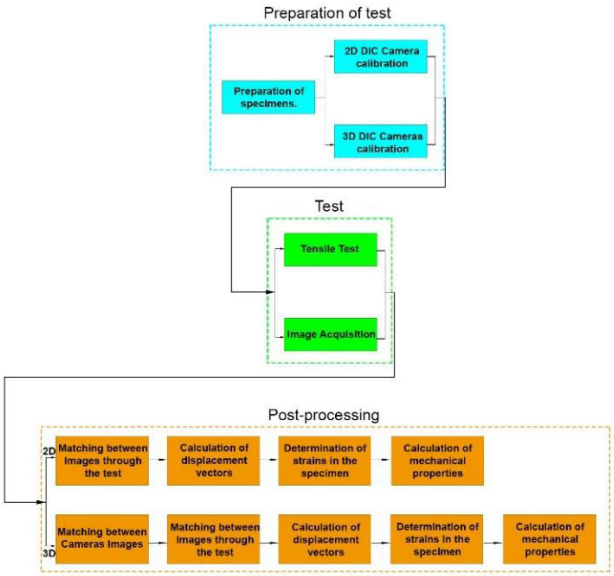

FIGURE 3. Workflow of the 2D and 3D DIC approach process.

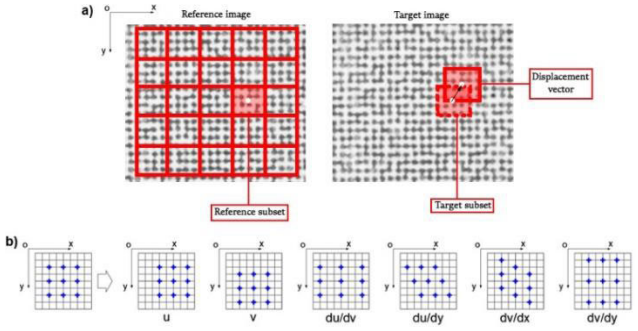

FIGURE 4. 2D DIC: a) calculation of the displacement vector and; b) degree of freedom considered for the strain calculation, u and v are the translation in the x and y direction; du/dys and dv/dx are the shear deformation through x and y directions.

the image coordinates corrected from lens distortion; k1, k2, k3 are the radial distortion parameters; and p1, p2 are the decentering distortion parameters.

After calibration, a set of images was processed using a 2D DIC approach (Figure 3) [51]. The DIC method divides the image into square regions, called sub-sets, which are compared between two consecutive images (i and i + 1), i being the reference image and i + 1 the deformed image. The calculation of displacements and strains of each subset started with the centroid determination in the deformed image (i + 1) with the use of [52]. The difference between the subset centroid positions provided the displacement vector, A, between the reference image (i) and the deformed image (i + 1) (Figure 4).

To reach sub-pixel precision in DIC, the Quintic B-spline function and a non-linear optimization has been carried out as it was described in past works [21], [53]. It is worth mentioning that the Inverse-Compositional Gauss-Newton

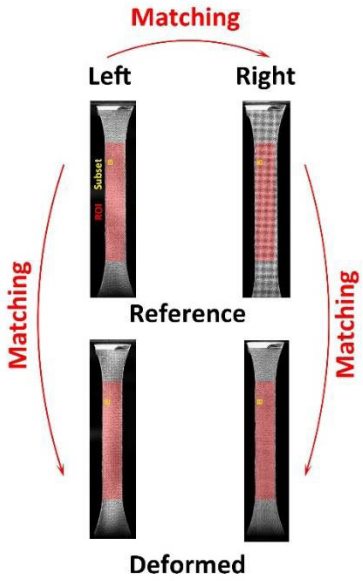

FIGURE 5. Matching between images through 3D DIC.

(IC-GN) algorithm was used for obtaining the solution to the optimisation problem. [54].

The strategy previously shown was applied over the entire Region of Interest (ROI). With the aim of minimizing the error propagation as well as optimizing the computation time, the reliability-guided digital image correlation algorithm (RG-DIC) was used [55].

2) 3D DIGITAL IMAGE CORRELATION

The main difference between 3D DIC and 2D DIC relies on the use of two or more additional cameras to estimate the displacements out of the main plane of the camera. To this end, the cameras need to be positioned in a non-orthogonal position [56]. In line with this, the 3D DIC method requires to solve the inner as well as the relative orientation of the cameras.

On the one hand, the inner calibration of the cameras was carried out using the 2D DIC calibration approach. Then, the relative orientation of the cameras was performed using the Direct Linear Transformation (DLT) [56], [57]. The use of the DLT allows to relate the image coordinates (xp, yp) with the object coordinates (X', Y', Z') (Eq. 2). With the aim of minimising the uncertainty along the depth-axis, a cylindrical calibration target with control points was used.

$$x_p = \frac{L_1X + L_2Y + L_3Z + L_4}{L_9X + L_{10}YL_{11}Z + 1}$$
$$y_p = \frac{L_5X + L_6Y + L_7Z + L_9}{L_9X + L_{10}YL_{11}Z + 1} \quad (2)$$

where x_p and y_p are the image point coordinates and $L_1 - L_{11}$ are the mathematical DLT parameters.

The relative orientation of the cameras allows them to obtain the 3D coordinates of homologous points which were determined in the following way (Figure 5): i) matching

between the pair of images (Left-Right); ii) matching between the images captured at the time i and i + 1 (Reference-Deformed). This matching was carried out in the same way that the 2D DIC. Then, the DLT transformation was applied in order to obtain the displacements of the subsets using the following least square approach (Eq. 3).

$$M = \left[A^T A\right]^{-1} A^T U \tag{3}$$

where **A** is a design matrix which connects the DLT parameters and the parameters presented in equation (2). **M** is the displacement matrix for every point. Finally, **U** is the difference matrix between DLT coordinates and camera parameters.

Thanks to this, it was possible to assess the in-plane displacements (x,y) and the out-of-plane movements (z) depth direction thanks to the use of the DLT. As a result, it was possible to obtain a 3D point cloud of the specimen evaluated which allowed to obtain the full-field displacements and strains using the 2D DIC approach previously defined.

D. STATISTICAL ANALYSIS

Once the process was finished following the 2D DIC and 3D DIC methods, parametric and non-parametric statistical analysis were performed to detect if there were significant differences among the mechanical properties. First, the data obtained for virtual extensometer in each experiment (DIC 2D and DIC 3D) were compared using the Kruskal-Wallis Test for independent samples. This non-parametric test allowed us to demonstrate whether a group of data comes from the same population.

If the existence of a statistically significant difference is not demonstrated, the parameters obtained with all the virtual extensometer for each experiment are compared using different parametric statistics: Levene Test and T-test. In addition, to strengthen the statistical comparison, non-parametric tests were applied: Median test, Kolmogorov-Smirnov, Moose's Test, Mann-Whitney U Test and Kruskal Wallis Test. These tests allowed us to evaluate the existence of statistically significant differences in each test.

E. NUMERICAL ANALYSIS

In order to evaluate how the material uncertainties (input) influence the numerical simulations (output), an advanced numerical strategy was followed. This strategy, which is based on a probabilistic approach, followed two stages: i) the definition of the numerical model and; ii) the reliability analysis.

1) DEFINITION OF THE NUMERICAL MODEL

A FEM model was implemented following the indications established in García-Martín *et al.* [21]. This numerical model consisted in a real case of repaired corroded steel pipe by a composite wrap made of different composite plies. This model required the definition of the following parts (Figure 6): i) the steel pipe; ii) the corroded part and iii) the wrap. The wrap part was meshed as a continuum

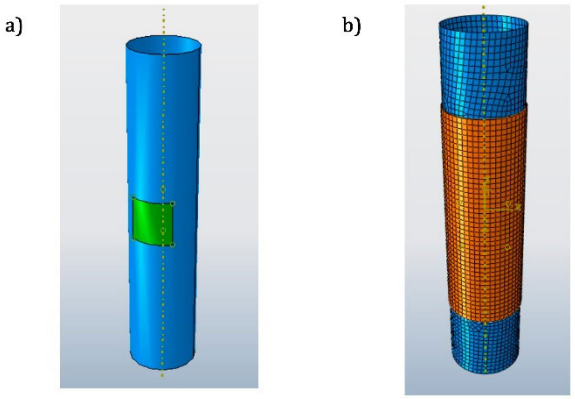

FIGURE 6. Numerical mesh used for evaluating the transmission of uncertainties: a) geometry and; b) numerical mesh. Blue areas correspond with the steel pipe without corrosion. The green area is representing the corrode zone and the orange areas the composite solution.

shell with reduced integration and eight nodes SC8R elements, obtaining a mesh with 5,779 elements. This model will be the start of the construction of the metamodel which will be explained later. And the final results are obtained because of the execution of this model. Also, this is a practical application of the material which is currently used in several simulations [58], [59].

The failure criterion of the models was the Tsai and Wu criterion [60]. This criterion assumes that failure occurs when the failure index (FI) is bigger than 1. Fi was calculated by the expression (Eq. 4):

$$\begin{aligned} FI = {} & F_1\sigma_1 + F_2\sigma_2 + F_3\sigma_3 + F_{11}\sigma_1^2 + F_{22}\sigma_2^2 + F_{33}\sigma_3^2 \\ & + 2F_{12}\sigma_1\sigma_2 + 2F_{23}\sigma_2\sigma_3 + 2F_{31}\sigma_3\sigma_1 + F_{44}\sigma_4^2 \\ & + F_{55}\sigma_5^2 + F_{66}\sigma_6^2 \leq 1 \end{aligned} \tag{4}$$

where:

$$F_1 = \frac{1}{X_T - \frac{1}{X_c}} \quad F_2 = \frac{1}{Y_T - \frac{1}{Y_c}} \quad F_3 = \frac{1}{Z_T - \frac{1}{Z_c}}$$

$$F_{11} = \frac{1}{X_T X_C} \quad F_{22} = \frac{1}{Y_T Y_C} \quad F_{33} = \frac{1}{Z_T Z_C}$$

$$F_{44} = \frac{1}{S_{yz}^2} \quad F_{55} = \frac{1}{S_{zx}^2} \quad F_{66} = \frac{1}{S_{xy}^2}$$

$$F_{12} = \left(-\frac{1}{2}\right)\sqrt{F_{11}F_{22}} \quad F_{23} = \left(-\frac{1}{2}\right)\sqrt{F_{22}F_{33}}$$

$$F_{31} = \left(-\frac{1}{2}\right)\sqrt{F_{33}F_{11}}$$

$\sigma_n \equiv$ Uniaxial tension in the different directions.
$X_T \equiv$ Tensile load
$X_C \equiv$ Compression load
$Y_T \equiv$ Transversal tensile load, in the y direction
$Z_T \equiv$ Transversal tensile load, in the z direction
$Y_C \equiv$ Transversal compression load, in the y direction
$Z_C \equiv$ Transversal compression load, in the z direction
$S_{xy}; S_{yz}; S_{zx} \equiv$ Shear transversal load

2) RELIABILITY ANALYSIS

As it was stated in the introduction, the proper analysis of composite materials requires the use of probabilistic approaches. These approaches allowed us to determine the probability of failure of a system (Eq. 5):

$$P_{f_k} = \int_{G_k(d,X)<0} f_X(X)\, dX \tag{5}$$

where:

- P_{fk} is the failure probability.
- G_k are the restrictions.
- $f_X(X)$ is the probability density function (PDF) of the random vector $X \in R^m$ and the design vector $d \in R^n$.

However, the solution to this equation is not trivial and requires the use of methods able to approximate this value. For the present case study it was decided to use the Monte Carlo method for approximating this value. This method requires the use of thousands of simulations in order to obtain reliable results, requiring a high computational cost. In order to solve this drawback, a metamodeling strategy was used, in our case the Polynomial Chaos Expansion (PCE) method [61]. This model shows a good performance on those systems with probabilistic inputs. The PCE approximates the behaviour of the numerical simulation using multivariate polynomials, assuming that the real model can be represented as a finite model whose inputs are considered independent variables [62]. In this way, the polynomials were constructed with respect to the PDFs of the independent input parameters by estimating their coefficients through least squares minimisation of the input variables and the real responses. In this case, the adaptive sparse PCE based on the least angle regression [63] was used along with the least angle regression algorithm [64], in order to avoid an over-fitting. In order to evaluate the quality of the metamodel obtained, the modified version of the Leave-one-out error (LOO) [65] was used (Eq. 6-7). This parameter allowed us to perform an estimation of the error with an acceptable computational cost.

$$LOOerror = \frac{1}{N}\sum_{i=1}^{N}\left(\frac{Y\left(X^{(i)} - f^{\sim PCE}\left(X^{i}\right)\right)}{1-h_i}\right)^2 \tag{6}$$

$$LOOerror^{*} = LOOerror * \left(1 - \frac{cardA}{N}\right)^{-1} \times \left(1 + tr\left(\varphi^T\varphi\right)^{-1}\right) \tag{7}$$

where $Y(X^{(i)})$ is the computational model; $f^{\sim PCE}(X^{(i)})$ is the surrogate model obtained from a specific DoE with N samples; h_i is the i-th diagonal term of the matrix $A(A^TA)^{-1}A^T$; **A** is the experimental matrix; *cardA* is the number of terms in the truncate series and; $\varphi = \{\varphi_{ij} = \varphi_j(x^{(i)}), i = 1, \ldots, N; j = 1, \ldots, cardA\}$.

All the process and simulations were executed using a Intel ®XEON E3-1240 v3 processor running at 3,4GHz with 8GB RAM DDRII.

TABLE 1. 2D DIC camera calibration parameters.

Parameters		Initial	Calibrated
Focal length (pixel)	fu	1.5310 x 104	1.5307 x 104
	fv	1.5307 x 104	1.5252 x 104
Principal point (pixel)	u	2.6224 x 103	2.6287 x 103
	v	1.8446 x 103	1.8372 x 103
Radial Distortion parameters	k1	0	-1.465 x 10-3
	k2	0	3.370 x 10-2
	k3	0	-1.450 x 10-5
Decentering distortion parameters	p1	0	1.252 x 10-5
	p2	0	-7.409 x 10-5

III. EXPERIMENTAL RESULTS

A total of 25 composite specimens were manufactured and tested specifically for this research. During each test the 2D and 3D DIC methods were simultaneously applied using the set-up described in the previous section. Thanks to this, it was possible to obtain different mechanical variables such as the Young Modulus (E), the Poisson ratio (v), and the maximum strength (T).

Previously to perform each test, the specimen was properly prepared according with the suggestion done in Section 2.1. In this case, we started with the specimen preparation applying the speckle pattern. It is worth mentioning that all the images were acquired in RAW format with the aim of enhancing the contrast during the post-processing stage, allowing a better correlation between subsets of different images until the fracture of the specimen. Please note that the cameras were synchronized to always shoot at the same time. The average Ground Sample Distance (GSD) was 0.07 mm/px in all the cases. The test speed was of 2 mm/min and the time among shoots was 2 seconds.

A. DIGITAL IMAGE CORRELATION RESULTS

1) 2D DIC APPROACH

The images acquired by the 2D DIC camera were firstly corrected from lens distortion using the pattern and calibration model defined in Section 2.3.2 (Table 1). To this end, a total of 74 images per specimen were used.

For the 2D DIC post-processing the open-source software Ncorr [66], developed in Matlab ©, was used. This software implements the procedures showed in Section 2, allowing to obtain full-field displacements and strains. During this stage a subset size of 20 × 20 pixels and a step of 7 pixels were used for calculating the full-field displacements. In order to obtain the mechanical properties of each specimen, a total of six virtual extensometers were placed on the surface. Three along the vertical direction and three along the horizontal direction. The first one was placed at the center of the Region of Interest (ROI), the other two were located at 3 mm of distance (Figure 7). Thanks to this, it was possible to obtain for each specimen a total of three Young Modulus (E) and Poisson's ratio (ν) and a maximum strain (T) (Figure 7). Furthermore, the full field of displacements was calculated in order to compare the 2D and 3D approaches (Figure 7B and 7C). Although the angular deviations in 2D-DIC can

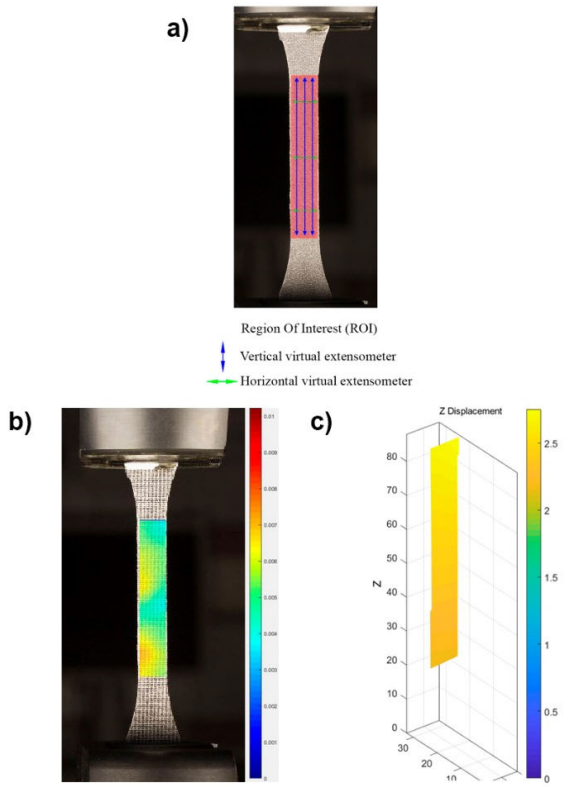

FIGURE 7. Fields of DIC into the specimen; a) Position of the different virtual extensometers used for each specimen; b) Field in the 2D DIC and c) Field in the 3D DIC reconstruction.

cause errors greater than 103 μ-strains [67], the procedure used to ensure the orthogonality avoided these errors and differences were not found with respect to the results obtained in 3D. The equality of outcome of both approaches also makes it possible to demonstrate that out-of-plane motions do not occur, something already known in plane tensile tests. Furthermore, a macro lens was used in order to minimize out-of-plane motion and that this does not contribute significantly to in-plane strain measurement error [31].

A non-parametric comparison was performed to analyze the existence of statistical significant differences between the calculated parameters (Young's Modulus (E) and Poisson's ratio (ν)) from each one of the three virtual extensometers within the 2D DIC experiment. For this purpose, a Kruskal Wallis test was applied between the E parameter of each virtual extensometer. This test did not demonstrate the existence of significant differences between extensometers in the variable E (p-value 0.938), nor for the variable v (p-value 0.694). Also, a parametric T-test was applied for E (p-value 0.950) and v (lower obtained p-value 0.259). The existence of significate statistical differences among the data provided by each virtual extensometer could not be demonstrated. Therefore, it was possible to work under the hypothesis that the data was homogeneous.

Finally, the PDF of each mechanical variable was computed, allowing to obtain the best PDF model. Then,

TABLE 2. 2D Results obtained from the specimens using 2D DIC approach.

Parameter	Number of data	Mean	Lower Bound	Upper Bound
E-Young's modulus (GPa)	75	51.7322	46.4217	56.9255
ν-Poisson's ratio (-)	75	0.0602	0.0176	0.1692
T-Maximum principal tensile (MPa)	25	484.849	465.107	506.858

TABLE 3. Goodness of fit (GOF) probability of the data obtained by 2D DIC approach; N-Normal, LN-Lognormal, W-Weibull, G-Gamma; 0-Accept and 1-Reject. Chi-Square (Chi), Kolmogorov-Smirnov (KS) and Anderson-Darling (AD) tests of the Young's Modulus (E), Poisson's ratio (ν) and Maximum principal tensile (T).

PDF	N			LN			W			G		
GOF	Chi	KS	AD	Chi	KS	AD	Chi	KS	AD	Chi	KS	AD
E	0	0	0	0	0	0	1	0	0	0	0	0
ν	1	0	0	0	0	0	1	1	1	0	0	0
T	0	0	0	0	0	0	0	0	0	0	0	0

TABLE 4. Principal parameters of the PDFs.

Parameter	Distribution	μ (Log-Normal)/A (Weibull)	σ(Log-Normal)/B(Weibull)
E	Log-Normal	3.9448	0.0515
ν	Log-Normal	-2.9025	0.4208
T	Weibull	442.0158	10.5146

the different statistics were calculated. Table 3 shows the results of using the Chi-square, Kolmogorov-Smirnov and Anderson-Darling tests.

Based on Table 3, Young Modulus (E) was adapted to a Log-Normal function (LN), Poisson ratio (ν) to a Log-Normal function (LN) and tensile strength (T) to a Weibull function (W). In order to reinforce this Figure 8 shows the graphic representation of the PDFs of each parameter. The principal values of the PDF distributions are shown in Figure 8.

Complementary to the estimation of the different PDF functions, a correlation analysis was carried out. For the present study case it was used the Spearman correlation index [68], [69]. This index varies from 1 (complete positive correlation), 0 (no correlation) and −1 (a complete inverse correlation) according with the following equation (Eq. 8):

$$rho = \frac{\sum (x - m_x)\left(y - m_y\right)}{\sqrt{\sum (x - m_x)^2 \sum \left(y - m_y\right)^2}} \tag{8}$$

where x and y are the two vectors of the different parameters and m_x and m_y are the corresponding means.

The correlation between parameters was shown in Table 5. According to this, it was possible to conclude that the Young

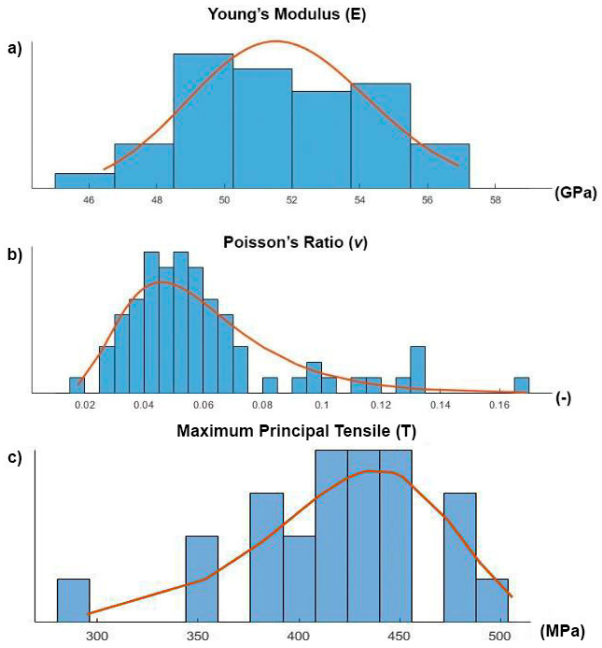

FIGURE 8. Graphical representation of the PDFs obtained by 2D DIC approach. a) Log-Normal distribution of the Young's Modulus (E); b) Log-Normal Distribution of the Poisson's Ratio (ν) and c) Weibull distribution of the Maximum principal tensile (T).

TABLE 5. Correlation matrix between parameters.

Spearman	E	ν	T
E	1	0.096	0.927
ν	0.096	1	0.043
T	0.927	0.043	1

Modulus (E) and the tensile strength (T) of the specimen were highly correlated (R2 $\cong$ 0.8527). Meanwhile the Poisson ratio (v) did not have correlation with the other two variables.

2) RESULTS FROM THE 3D DIC

For the 3D DIC post-processing the open-source software MultiDIC was used [70]. This software is based on Ncorr [64], using the same algorithms for processing the displacements and strains but including the relative orientation of the cameras.

Firstly, the inner calibration of the cameras was obtained by applying the method used in the previous section, obtaining the following results (Table 6).

Then the relative orientation of the cameras was obtained using the inner calibration parameters as well as the cylindrical calibration target showed in Section 2.3.2 to solve the DLT transformation. These parameters allowed us to reconstruct the position of each subset's centroid in 3D and thus their displacement vector as the difference of the centroid in the pair of images i (reference) and the pair of images i + 1 (deformed).

Similarly to the 2D DIC, during the 3D DIC reconstruction a total of six extensometers placed in the same position were used. Thanks to this it was possible to obtain a set of values of the Young Modulus (E), Poisson ratio (v) and maximum strain (T) (Table 7). These values were used to calculate the PDF functions following the method used in the previous section (Table 8, Table 9) (Figure 9).

TABLE 6. 3D DIC cameras calibration parameters.

Parameter		Camera 1		Camera 2	
		Initial	Calibrated	Initial	Calibrated
Focal length (pixel)	fu	1.5247 x 104	1.5256 x 104	1.5345 x 104	1.5346 x 104
	fv	1.5230 x 104	1.5239 x 104	1.5327 x 104	1.5328 x 104
Principal point (pixel)	u	2.6196 x 103	2.6264 x 103	2.6329 x 103	2.6294 x 103
	v	1.8309 x 103	1.8299 x 103	1.8473 x 103	1.8473 x 103
Radial Distortion	k1	0	-1.861 x 10-4	0	7.944 x 10-5
	k2	0	3.591 x 10-2	0	-3.763 x 10-3
	k3	0	-1.143	0	0.1687
Tangential distortion	p1	0	-2.078 x 10-5	0	-5.237 x 10-7
	p2	0	7.772 x 10-5	0	-7.245 x 10-5

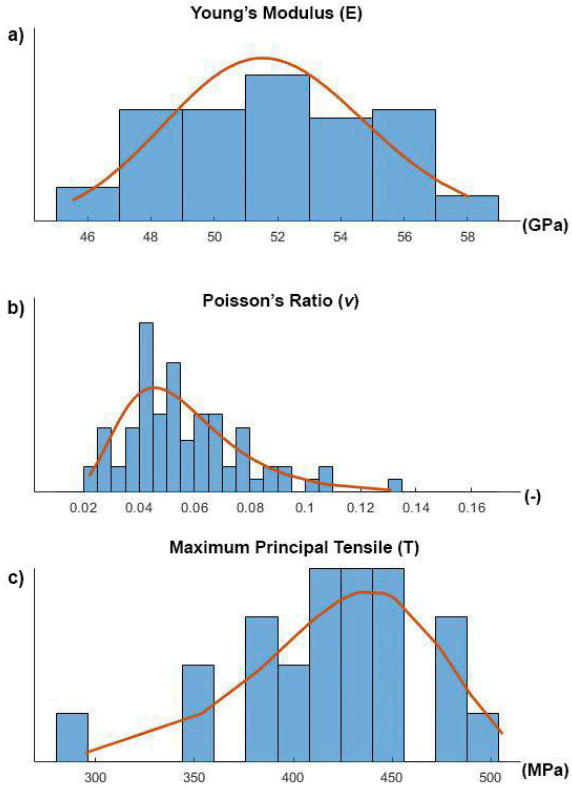

FIGURE 9. Graphical representation of the PDFs obtained by 3D DIC approach. a) Log-Normal distribution of the Young's Modulus (E); b) Log-Normal Distribution of the Poisson's Ratio (ν) and c) Weibull distribution of the Maximum principal tensile (T).

TABLE 7. Results obtained from the specimens using 3D DIC approach.

Parameter	Number of data	Mean	Lower Bound	Upper Bound
E-Young's modulus (GPa)	75	53.9820	48.5101	59.9470
ν-Poisson's ratio (-)	75	0.0626	0.0183	0.1760
T-Maximum principal tensile (MPa)	25	484.849	465.107	506.858

TABLE 8. Goodness of fit (GOF) probability of the data obtained by 3D DIC approach; N-Normal, LN-Lognormal, W-Weibull, G-Gamma; 0-Accept and 1-Reject. Chi-Square (Chi), Kolmogorov-Smirnov (KS) and Anderson-Darling (AD) tests of the Young's Modulus (E), Poisson's ratio (v) and Maximum principal tensile (T).

PDF	N			LN			W			G		
GOF	Chi	KS	AD	Chi	KS	AD	Chi	KS	AD	Chi	KS	AD
E	0	0	0	0	0	0	1	0	0	0	0	0
ν	1	1	1	0	0	0	1	1	1	0	0	0
T	0	0	0	0	0	0	0	0	0	0	0	0

TABLE 9. Principal parameters of the PDFs.

Parameter	Distribution	μ (Log-Normal)/A (Weibull)	σ(Log-Normal)/B(Weibull)
E	Log-Normal	3.9871	0.0564
ν	Log-Normal	-2.8616	0.4186
T	Weibull	442.0158	10.5146

TABLE 10. Spearman correlation factor.

Spearman	E	ν	T
E	1	0.036	0.890
ν	0.036	1	0.043
T	0.890	0.043	1

A non-parametric comparison was performed to analyse the existence of statistically significant differences between the calculated parameters (E and T) from each one of the three virtual extensometers within the 3D DIC experiment. For this purpose, a Kruskal Wallis Test was applied first. This test did not demonstrate the existence of significant differences among the extensometers for the variable E (p-value 0.820) nor for the variable ν (p-value 0.693). Also, a parametric T-test was applied for E (p-value 0.805) and ν (p-value 0.277). The existence of statistically significate differences between the data of each virtual extensometer could not be demonstrated. Therefore, it was possible to work under the hypothesis that the data was homogeneous.

As it was done in the previous section, the Spearman correlation factor was calculated (Table 10).

TABLE 11. Comparisons between PDFs of Young's Modulus (E), Poisson's ratio (*ν*) of the specimens obtained by 2D DIC and 3D DIC.

		DIC 2D	DIC 3D
E, Young's Modulus (GPa)	Mean	51.7322	53.9820
	Median	51.6140	53.4880
	Lower Bound	46.4217	48.5101
	Upper bound	56.9255	59.9470
	PDF	Log-Normal	
	μ	3.9448	3.9871
	σ	0.0515	0.0564
ν, Poisson coefficient (-)	Mean	0.0602	0.0626
	Median	0.0537	0.0555
	Lower Bound	0.0176	0.0183
	Upper Bound	0.1692	0.1760
	PDF	Log-normal	
	μ	-2.9025	-2.8616
	σ	0.4208	0.4186
Spearman correlation	E-T	0.927	0.890
	E-ν	0.096	0.036
	ν-T	0.043	0.043

The R^2 between E and T was 0.6989 and the RSME was 26.41.

Table 11 shows a comparison between the PDFs obtained by the 2D DIC and the 3D DIC.

B. STATISTICAL COMPARISON

As it was noted in the previous sections, significant differences were not detected between the data provided by each of the three virtual extensometers (within the same experiment). Therefore, using the results of all virtual extensometer, a general statistical comparison between 2D DIC and 3D DIC, can be made using parametric and non-parametric methods. The parametric statistics applied were Levene Test to study equality of variances, and the T-test to study equality of means. The non-parametric statistics applied were the Median Equality Test and the Moses Test. To analyze the equality of the distribution, the Mann-Whitney U Test, the Kolmogorov-Smirnov Test (K-S) and the Kruskal Wallis Test were used. The results are shown in the Table 12.

For the variable E, both parametric and non-parametric tests indicate that there are statistically significant differences ($p < 0.05$), except in the case of equality of variances. For the variable ν, the existence of significant differences between the two methods cannot be demonstrated. The histogram of both variables can be visualised in Figure 10, observing a significate difference in the central tendency for the

TABLE 12. P-value of the different test applied to compare the two experiments.

	Parametric test		Non-parametric test				
	Variances equality (Levene)	Means equality T test	Median equality test	Range equality (Moses)	Distribution equality		
					U-Mann-Whitney	K-S	Kruskal-Wallis
E	0.104	0.000	0.009	0.000	0.000	0.003	0.000
v	0.856	0.613	0.514	0.610	0.442	0.97	0.442

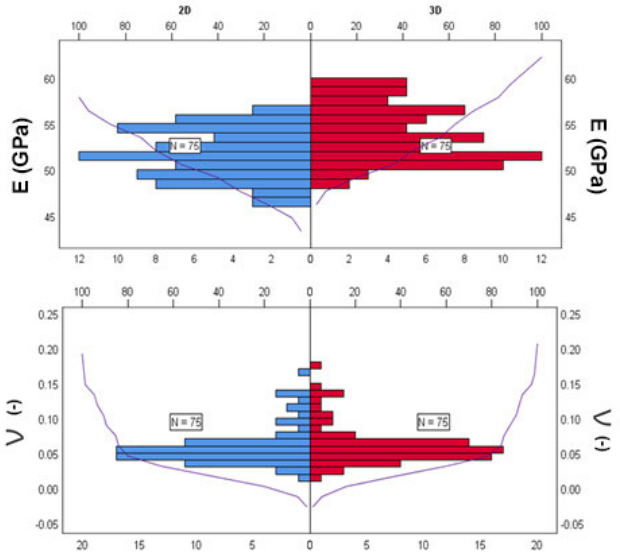

FIGURE 10. Histogram of the variable E (up) and ν (down) obtained for each method DIC 2D and DIC 3D. In blue is represented the histogram obtained by the 2D method and in red the histogram obtained by the 3D strategy. The purple line represents the accumulated.

variable E. These significant differences can be explained from the point of view of the different uncertainties of each of the methods used. While in the 2D approach the main source of uncertainty are out-of-plane strains, in the 3D approach they are mostly related to the calibration of the cameras. This means that although the test procedures are similar, the uncertainties are independent for each technique. In this case, the difference between the strains is approximately 10-4 for values of an order of 20 times greater, so it is acceptable.

C. GLOBAL RELIABILITY ANALYSIS

From the results previously obtained, a global reliability analysis was performed over the deterministic mesh considering the Young Modulus, E, and the Poisson's coefficient, v, obtained in 2D DIC and 3D DIC as the input variables. As it was described in section 2.5, it was necessary to have a tool to determinate the Tsai Wu maximum in every simulation. So, for this reason a FEM analysis was executed.

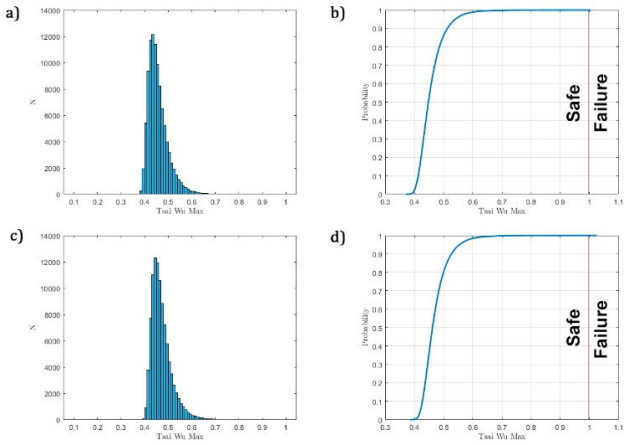

FIGURE 11. Metamodelling results: a) Tsai-Wu distribution in the 2D DIC metamodel simulations; b) Cumulative distribution function of the 2D-DIC metamodeling simulations; c) Tsai-Wu distribution in the 3D DIC metamodel simulations; b) Cumulative distribution function of the 3D-DIC metamodel simulations.

TABLE 13. Quartile and percentile Tsai Wu analysis with parameters obtained by 2D DIC and 3D DIC.

	Tsai Wu	
	2D DIC	3D DIC
Quartile 1	0.4269	0.4412
Quartile 2	0.4478	0.4619
Quartile 3	0.4769	0.4908
Quartile 4	1.0046	1.0254
IQR	0.0500	0.0496
IPR80%	0.0977	0.0944
IPR90%	0.1341	0.1339

After that, a metamodel was built. In this way, the computer cost was greatly reduced, and it was possible to carry out a huge number of simulations in less time. As it was commented in section 2.5.2, the LOO error results obtained by the different metamodels were 0.032 in the 2D DIC methodology and 0.0034 in the 3D DIC methodology.

A total of 200 executions to build the metamodel were carried out, and then a total of 100,000 executions of the Reliability analysis were carried out obtaining the probability of failure and the concentration of that as it is shown in Figure 11, where it was compared the probability with the parameters obtained by 2D DIC and 3D DIC.

After the simulations, in the 2D and 3D only one case of 100,000 provided a Tsai Wu higher than 1. Next table (Table 13) outlines the Tsai Wu values at different quartiles.

The inter-quartile (IQR) and inter-percentile (IPR) ranges (Table 13) were extracted from the data generated in the Tsai-Wu analysis. The data show that the distribution for 2D DIC and 3D DIC are similar. This can be corroborated

through the visualization of the histogram and failure plot (Figure 11).

IV. CONCLUSION

This work aims to compare two DIC methods for determining the mechanical properties of CFRP composite solutions. To this end, a total of 25 composite specimens were tested using 3 different cameras at the same time: one for the 2D DIC method and two for the 3D DIC. The mechanical properties of the composite were determined using virtual extensometers in each one of the samples. Then, the Young Modulus, E, and Poisson ratio, v, were extracted. The Kruskal Wallis test performed on each of these variables reveals that the data captured is homogenous and could be considered as a unique population: one for the Young Modulus, E, and one for the Poisson ratio, v. According with different parametric and non-parametric tests performed, significant differences for the Young Modulus, E, were detected between the two tests. Specifically, the mean and median of the Young Module obtained by 3D-DIC was slightly higher than the one obtained by 2D-DIC. Despite this, the differences obtained were acceptable and may be due to the uncertainties of each test setup.

Finally, a set of probabilistic numerical analysis were carried out with the aim of analysing the discrepancies in the numerical simulations for a real study case, fed by a FEM model, simulating a repaired corroded pipe. To this end it was used the PDF functions of each variable, as well as a metamodeling strategy for reducing the computational costs since it was required to perform a Monte Carlo analysis. The results obtained in both numerical analyses revealed a great similarity between both approaches in terms of interquartile, accumulative histograms and probability of failure. Also, a statistical comparison between the principal mechanical properties shows the same similarity. These results show that the small differences found between 2D and 3D are no longer significant when probabilistic numerical analysis methods are applied. In this way, the uncertainties are blurred and similar valid results are obtained for both methods, since the validity of the 2D-DIC method has been verified in previous works.

In accordance with the results obtained during this work it was possible to conclude that the 3D DIC method was able to provide similar results than the 2D DIC with the advantage of being possible its use in non-planar surfaces. These surfaces were used for the determination of the mechanical properties in CFRP solutions.

Future works will be focused on integrating the 3D approach in all the design chain, starting from the mechanical characterization and ending in the verification of the numerical model using physical specimens.

REFERENCES

[1] N. Yahaya, N. M. Noor, S. Rabe'ah Ot, L. K. Sing, and M. M. Din, "New technique for studying soil-corrosion of underground pipeline," *J. Appl. Sci.*, vol. 11, no. 9, pp. 1510–1518, Apr. 2011.

[2] J. L. Alamilla, M. A. Espinosa-Medina, and E. Sosa, "Modelling steel corrosion damage in soil environment," *Corrosion Sci.*, vol. 51, no. 11, pp. 2628–2638, Nov. 2009.

[3] A. Vedrtnam, "Novel method for improving fatigue behavior of carbon fiber reinforced epoxy composite," *Compos. B, Eng.*, vol. 157, pp. 305–321, Jan. 2019.

[4] P. R. Vieira, E. M. L. Carvalho, J. D. Vieira, and R. D. T. Filho, "Experimental fatigue behavior of pultruded glass fibre reinforced polymer composite materials," *Compos. B, Eng.*, vol. 146, pp. 69–75, Aug. 2018.

[5] S. S. R. Koloor, M. A. Abdullah, M. N. Tamin, and M. R. Ayatollahi, "Fatigue damage of cohesive interfaces in fiber-reinforced polymer composite laminates," *Compos. Sci. Technol.*, vol. 183, Oct. 2019, Art. no. 107779.

[6] S. B. Bati and T. Rotunno, "Environmental durability of the bond between the CFRP composite materials and masonry structures," *Hist. Construct.*, vol. 1039, p. 46, Nov. 2001.

[7] G. B. Sinclair and J. E. Helms, "A review of simple formulae for elastic hoop stresses in cylindrical and spherical pressure vessels: What can be used when," *Int. J. Pressure Vessels Piping*, vol. 128, pp. 1–7, Apr. 2015.

[8] P. J. I. F. W. P. Laney, "Use of composite pipe materials in the transportation of natural gas," INEEL Field Work Proposal, Tech. Rep. 4340-70, 2002.

[9] N. D. Hai and H. Mutsuyoshi, "Structural behavior of double-lap joints of steel splice plates bolted/bonded to pultruded hybrid CFRP/GFRP laminates," *Construct. Building Mater.*, vol. 30, pp. 347–359, May 2012.

[10] M. Mokhtari and A. A. Nia, "The application of CFRP to strengthen buried steel pipelines against subsurface explosion," *Soil Dyn. Earthq. Eng.*, vol. 87, pp. 52–62, Aug. 2016.

[11] R. Rafiee, "On the mechanical performance of glass-fibre-reinforced thermosetting-resin pipes: A review," *Compos. Struct.*, vol. 143, pp. 151–164, May 2016.

[12] C. Colombo and L. Vergani, "Optimization of filament winding parameters for the design of a composite pipe," *Compos. B, Eng.*, vol. 148, pp. 207–216, Sep. 2018.

[13] O. Orell, J. Vuorinen, J. Jokinen, H. Kettunen, P. Hytönen, J. Turunen, and M. Kanerva, "Characterization of elastic constants of anisotropic composites in compression using digital image correlation," *Compos. Struct.*, vol. 185, pp. 176–185, Feb. 2018.

[14] J. S. Berg and D. F. Adams, "An evaluation of composite material compression test methods," *J. Compos., Technol. Res.*, vol. 11, no. 2, pp. 41–46, 1989.

[15] C. Barile, C. Casavola, and F. De Cillis, "Mechanical comparison of new composite materials for aerospace applications," *Compos. B, Eng.*, vol. 162, pp. 122–128, Apr. 2019.

[16] T. He, L. Liu, and A. Makeev, "Uncertainty analysis in composite material properties characterization using digital image correlation and finite element model updating," *Compos. Struct.*, vol. 184, pp. 337–351, Jan. 2018.

[17] C. T. Sun and R. S. Vaidya, "Prediction of composite properties from a representative volume element," *Compos. Sci. Technol.*, vol. 56, no. 2, pp. 171–179, Jan. 1996.

[18] M. Nirbhay, A. Dixit, R. Misra, and H. S. Mali, "Tensile test simulation of CFRP test specimen using finite elements," *Proc. Mater. Sci.*, vol. 5, pp. 267–273, Jan. 2014.

[19] S. Joshi and S. M. Harle, "Linear variable differential transducer (LVDT) & its applications in civil engineering," *Int. J. Transp. Eng. Technol.*, vol. 3, no. 4, pp. 62–66, 2017.

[20] R. Garcia-Martin, Á. Bautista-De Castro, L. J. Sánchez-Aparicio, J. G. Fueyo, and D. Gonzalez-Aguilera, "Combining digital image correlation and probabilistic approaches for the reliability analysis of composite pressure vessels," *Arch. Civil Mech. Eng.*, vol. 19, no. 1, pp. 224–239, Mar. 2019.

[21] R. García-Martin, J. López-Rebollo, L. J. Sánchez-Aparicio, J. G. Fueyo, J. Pisonero, and D. González-Aguilera, "Digital image correlation and reliability-based methods for the design and repair of pressure pipes through composite solutions," *Construct. Building Mater.*, vol. 248, Jul. 2020, Art. no. 118625.

[22] M. A. Seif, U. A. Khashaba, and R. Rojas-Oviedo, "Measuring delamination in carbon/epoxy composites using a shadow moiré laser based imaging technique," *Compos. Struct.*, vol. 79, no. 1, pp. 113–118, Jun. 2007.

[23] C. Gallage and C. P. G. Jayalath, "Use of particle image velocimetry (PIV) technique to measure strains in geogrids," in *Proc. 7th Int. Symp. Deformation Characteristics Geomaterials (IS-Glasgow)(E3S Web Conf.*, vol. 92. Les Ulis, France: EDP Sciences, 2019, pp. 1–6.

[24] I. Rullman, M. Patyna, B. Janssen, and B. Willershausen, "Determination of polymerization shrinkage of different composites using a photoelastic method," *Amer. J. Dentistry*, vol. 30, no. 1, pp. 16–22, 2017.
[25] M. T. Arellano, L. Crouzeix, B. Douchin, F. Collombet, H. H. Moreno, and J. G. Velázquez, "Strain field measurement of filament-wound composites at ±55° using digital image correlation: An approach for unit cells employing flat specimens," *Compos. Struct.*, vol. 92, no. 10, pp. 2457–2464, Sep. 2010.
[26] T. C. Chu, W. F. Ranson, and M. A. Sutton, "Applications of digital-image-correlation techniques to experimental mechanics," *Experim. Mech.*, vol. 25, no. 3, pp. 232–244, Sep. 1985.
[27] Y. He, A. Makeev, and B. Shonkwiler, "Characterization of nonlinear shear properties for composite materials using digital image correlation and finite element analysis," *Compos. Sci. Technol.*, vol. 73, pp. 64–71, Nov. 2012.
[28] A. Villarino, J. López-Rebollo, and N. Antón, "Analysis of mechanical behavior through digital image correlation and reliability of *Pinus halepensis* Mill," *Forests*, vol. 11, no. 11, p. 1232, Nov. 2020.
[29] E. Teijón-López-Zuazo, J. López-Rebollo, L. J. Sánchez-Aparicio, R. Garcia-Martín, and D. Gonzalez-Aguilera, "Compression and strain predictive models in non-structural recycled concretes made from construction and demolition wastes," *Materials*, vol. 14, no. 12, p. 3177, Jun. 2021.
[30] A. J. Comer, K. B. Katnam, W. F. Stanley, and T. M. Young, "Characterising the behaviour of composite single lap bonded joints using digital image correlation," *Int. J. Adhes. Adhesives*, vol. 40, pp. 215–223, Jan. 2013.
[31] M. A. Sutton, J. H. Yan, V. Tiwari, H. W. Schreier, and J. J. Orteu, "The effect of out-of-plane motion on 2D and 3D digital image correlation measurements," *Opt. Lasers Eng.*, vol. 46, no. 10, pp. 746–757, 2008.
[32] M. A. Caminero, M. Lopez-Pedrosa, C. Pinna, and C. Soutis, "Damage monitoring and analysis of composite laminates with an open hole and adhesively bonded repairs using digital image correlation," *Compos. B, Eng.*, vol. 53, pp. 76–91, Oct. 2013.
[33] B. Pan, "Digital image correlation for surface deformation measurement: Historical developments, recent advances and future goals," *Meas. Sci. Technol.*, vol. 29, no. 8, Aug. 2018, Art. no. 082001.
[34] M. Frieß, M. Scheiffele, W. Zankl, and F. J. P. O. H.-C. Hofmann, "Development, manufacture and characterization of C/C-SiC components based on filament winding," in *Proc. HT-CMC*, 2010, pp. 92–97.
[35] A. F. Hamed, M. M. Hamdan, B. B. Sahari, and S. M. Sapuan, "Experimental characterization of filament wound glass/epoxy and carbon/epoxy composite materials," *ARPN J. Eng. Appl. Sci.*, vol. 3, no. 4, pp. 76–87, 2008.
[36] C. V. Reddy, P. R. Babu, R. Ramnarayanan, and D. Das, "Mechanical characterization of unidirectional carbon and glass/epoxy reinforced composites for high strength applications," *Mater. Today, Proc.*, vol. 4, no. 2, pp. 3166–3172, 2017.
[37] A. L. Gol'Denveizer, *Theory of Elastic Thin Shells: Solid and Structural Mechanics*. Amsterdam, The Netherlands: Elsevier, 2014.
[38] *Plastics-Determination of Tensile Properties—Part 4: Test Conditions for Isotropic and Orthotropic Fibre-Reinforced Plastic Composites*, Standard E. ISO, 527-4., International Organization for Standardization (ISO), Geneva, Switzerland, 1997.
[39] *Determination of Tensile Properties—Part 4: Test Conditions for Isotropic and Orthotropic Fibre-Reinforced Plastic Composites. European Standard*, Standard E. ISO, 527-4, International Organization for Standardization, 1997.
[40] B. Pan, L. Yu, and D. Wu, "High-accuracy 2D digital image correlation measurements with bilateral telecentric lenses: Error analysis and experimental verification," *Experim. Mech.*, vol. 53, no. 9, pp. 1719–1733, Nov. 2013.
[41] E. Byrne and M. J. C. S. K. A. H. W. C. C. S. I. P. Simonsen, "Lens selection and stereo angle," *Correl. Solut. Knowledgebase*, 2016.
[42] Y. Dong and B. Pan, "A review of speckle pattern fabrication and assessment for digital image correlation," *Exp. Mech.*, vol. 57, no. 8, pp. 1161–1181, Oct. 2017.
[43] P. Reu, "All about speckles: Aliasing," *Experim. Techn.*, vol. 38, no. 5, pp. 1–3, Sep. 2014.
[44] P. Reu, "All about speckles: Speckle size measurement," *Experim. Techn.*, vol. 38, no. 6, pp. 1–2, Nov. 2014.
[45] P. Reu, "All about speckles: Contrast," *Exp. Tech.*, vol. 39, no. 1, pp. 1–2, 2015.
[46] P. Reu, "All about speckles: Edge sharpness," *Experim. Techn.*, vol. 39, no. 2, pp. 1–2, Mar. 2015.
[47] D. Lecompte, A. Smits, S. Bossuyt, H. Sol, J. Vantomme, D. Van Hemelrijck, and A. M. Habraken, "Quality assessment of speckle patterns for digital image correlation," *Opt. Lasers Eng.*, vol. 44, no. 11, pp. 1132–1145, Nov. 2006.
[48] B. Pan, Z. Lu, and H. Xie, "Mean intensity gradient: An effective global parameter for quality assessment of the speckle patterns used in digital image correlation," *Opt. Lasers Eng.*, vol. 48, no. 4, pp. 469–477, Apr. 2010.
[49] T. Hua, H. Xie, S. Wang, Z. Hu, P. Chen, and Q. Zhang, "Evaluation of the quality of a speckle pattern in the digital image correlation method by mean subset fluctuation," *Opt. Laser Technol.*, vol. 43, no. 1, pp. 9–13, 2011.
[50] C.-C. Ho, D.-S. Wu, Y.-J. Chang, J.-C. Hsu, C.-L. Kuo, and S.-K. Kuo, "Experimental investigation of speckle pattern by laser scribing for digital image correlation," *J. Laser Micro Nanoeng.*, vol. 12, no. 2, p. 97, 2017.
[51] H. Lu and P. D. Cary, "Deformation measurements by digital image correlation: Implementation of a second-order displacement gradient," *Exp. Mech.*, vol. 40, no. 4, pp. 393–400, 2000.
[52] J.-C. Yoo and T. H. Han, "Fast normalized cross-correlation," *Circuits, Syst. Signal Process.*, vol. 28, pp. 819–843, Dec. 2009.
[53] M. Unser, "Splines: A perfect fit for signal and image processing," *IEEE Signal Process. Mag.*, vol. 16, no. 6, pp. 22–38, Nov. 1999.
[54] P. Bing, X. Hui-Min, X. Bo-Qin, and D. Fu-Long, "Performance of sub-pixel registration algorithms in digital image correlation," *Meas. Sci. Technol.*, vol. 17, no. 6, p. 1615, 2006.
[55] B. Pan, W. Dafang, and X. Yong, "Incremental calculation for large deformation measurement using reliability-guided digital image correlation," *Opt. Lasers Eng.*, vol. 50, no. 4, pp. 586–592, Apr. 2012.
[56] Z. Xiao, J. Liang, D. Yu, Z. Tang, and A. Asundi, "An accurate stereo vision system using cross-shaped target self-calibration method based on photogrammetry," *Opt. Lasers Eng.*, vol. 48, no. 12, pp. 1252–1261, Dec. 2010.
[57] D. Gonzalez-Aguilera, L. López-Fernández, P. Rodriguez-Gonzalvez, D. Hernandez-Lopez, D. Guerrero, F. Remondino, F. Menna, E. Nocerino, I. Toschi, A. Ballabeni, and M. Gaiani, "GRAPHOS—Open-source software for photogrammetric applications," *Photogramm. Rec.*, vol. 33, no. 161, pp. 11–29, Mar. 2018.
[58] E. Mahdi and E. Eltai, "Development of cost-effective composite repair system for oil/gas pipelines," *Compos. Struct.*, vol. 202, pp. 802–806, Oct. 2018.
[59] H. S. D. C. Mattos, J. M. L. Reis, L. M. Paim, M. L. D. Silva, R. L. Junior, and V. A. Perrut, "Failure analysis of corroded pipelines reinforced with composite repair systems," *Eng. Failure Anal.*, vol. 59, pp. 223–236, Jan. 2016.
[60] S. W. Tsai and E. M. Wu, "A general theory of strength for anisotropic materials," *J. Compos. Mater.*, vol. 5, no. 1, pp. 58–80, Jan. 1971.
[61] L. Novak and D. Novak, "Polynomial chaos expansion for surrogate modelling: Theory and software," *Beton-Und Stahlbetonbau*, vol. 113, pp. 27–32, Sep. 2018.
[62] N. Wiener, "The homogeneous chaos," *Amer. J. Math.*, vol. 60, no. 4, pp. 897–936, 1938.
[63] G. Blatman and B. Sudret, "Adaptive sparse polynomial chaos expansion based on least angle regression," *J. Comput. Phys.*, vol. 230, no. 6, pp. 2345–2367, Mar. 2011.
[64] B. Efron, T. Hastie, I. Johnstone, and R. Tibshirani, "Least angle regression," *Ann. Statist.*, vol. 32, no. 2, pp. 407–499, 2004.
[65] G. Deman, K. Konakli, B. Sudret, J. Kerrou, P. Perrochet, and H. Benabderrahmane, "Using sparse polynomial chaos expansions for the global sensitivity analysis of groundwater lifetime expectancy in a multi-layered hydrogeological model," *Rel. Eng. Syst. Saf.*, vol. 147, pp. 156–169, Mar. 2016.
[66] J. Blaber, B. Adair, and A. Antoniou, "Ncorr: Open-source 2D digital image correlation MATLAB software," *Exp. Mech.*, vol. 55, no. 6, pp. 1105–1122, 2015.
[67] A. Hijazi, A. Friedl, and C. J. J. Kähler, "Influence of camera's optical axis non-perpendicularity on measurement accuracy of two-dimensional digital image correlation," *JJMIE*, vol. 5, no. 4, pp. 1–10, 2011.
[68] C. Wissler, "The Spearman correlation formula," *Science*, vol. 22, no. 558, pp. 309–311, Sep. 1905.
[69] C. Croux and C. Dehon, "Influence functions of the Spearman and Kendall correlation measures," *Stat. Methods Appl.*, vol. 19, no. 4, pp. 497–515, Nov. 2010.
[70] D. Solav, K. M. Moerman, A. M. Jaeger, K. Genovese, and H. M. Herr, "MultiDIC: An open-source toolbox for multi-view 3D digital image correlation," *IEEE Access*, vol. 6, pp. 30520–30535, 2018.

JAVIER PISONERO received the degree in mechanical engineering and the master's degree in renewable energy and energy efficiency from the University of Salamanca, Spain, in 2017 and 2018, respectively. He was a Project Participant in the Interreg Sudoe platform in collaboration with state companies and the universities of Aveiro and Bordeaux. He obtained the award for the first record of the promotion during his degree at the University of Salamanca.

JORGE LÓPEZ-REBOLLO graduate in civil engineering (specializing in hydrology) from the Higher Polytechnic School of Ávila, University of Salamanca, in 2018. During the 2017/18 academic year, he obtained a Collaboration Grant from the Department of Construction and Agronomy, USAL, for the project ''Geometric optimization of bridges at the scale of laminated wood.'' He obtained the ''Extraordinary Prize'' with his Final Degree Project titled ''Determination of the mechanical properties of aleppo pine wood (Pinus halepensis) from the compression test and the digital image correlation.''

ROBERTO GARCÍA-MARTÍN received the degree in industrial engineering and the degree in materials engineering from the University of Salamanca. Since 1998, he has been a Professor attached to the mechanical engineering area, where he currently teaches in the degree of mechanical engineering as well as in the degree of renewable energies and energy efficiency at the University of Salamanca. He also leads several research projects in collaboration with companies in the region. His research interest includes the use of applied geotechnologies for the development and verification of composite materials.

MANUEL RODRÍGUEZ-MARTÍN was born in Ávila, Spain, in 1988. He received the B.S. degree in mechanical engineering from the University of Valladolid, Spain, in 2010, the B.S. degree in industrial engineering from Nebrija University, Spain, in 2011, the M.S. degree in mechanical engineering from the University of Salamanca, Avila, in 2012, and the Ph.D. degree from the University of Salamanca, Avila, and the University of Vigo, Vigo, Spain, in 2015. He has been working as a Freelance Engineer, since 2012, a Researcher and a Developer at the spin-off company ITOS 3D, since 2014, and a Postdoctoral Researcher at the TIDOP Research Group, University of Salamanca, since 2015. He currently works as an Assistant Professor with the Department of Mechanical Engineering, University of Salamanca. He has authored numerous research works which have been published in international journals, books, and conference proceedings. Additionally, he has managed and participated in several research projects and patents inventions. His research interests include novel quality inspection and testing methods based on image, thermal, and remote sensors.

LUIS JAVIER SÁNCHEZ-APARICIO received the bachelor's degree in architecture, in 2011, the master's degree in geotechnologies applied to architecture and engineering, in 2012, the degree in building engineering, in 2014, and the Ph.D. degree *(cum laude)*, in 2016. This year, he did a pre-doctoral stay during six months at the University of Minho, Guimarães, Portugal, with the Research Group of Masonry and Historical Constructions, with which he remains research collaborations. He is currently an Assistant Professor at the Department of Construction and Building Technology, Universidad Politécnica de Madrid. He has 40 research publications with more than 20 JCR papers. He has participated in several international and national project related with the preservation of heritage and material characterization by means of the digital image correlation method. He received the International Mention And Extraordinary Prize for his Ph.D. degree. He has received several research awards, such as the Coello '20 or the GEICC '19.

A. MUÑOZ-NIETO received the degree in surveying engineering from the University of Extremadura and the Ph.D. degree in geography from the University of Salamanca, in 2008. Since 1991, he has been an Associate Professor in the field of geodesy, photogrammetry and cartography engineering. He is currently the Director of the Department of Cartographic and Land Engineering and the University of Salamanca. He teaches in the degree in geomatics and topography and civil engineering as well as in the master's in cartographic geotechnologies and oenology and their adaptation to climate change. His research interests primarily include the use of mapping geotechnologies for documentation and dissemination of heritage as well as the integration of sensors for 3-D modeling of complex scenarios.

DIEGO GONZÁLEZ-AGUILERA graduated in surveying engineering and geodesy and cartography engineering from Salamanca University, Spain, in 1999 and 2001, respectively. He received the Ph.D. degree in 3D reconstruction from a single view from the Institute of Computer Vision and Robotics, INRIA, Grenoble, France, in 2005. He stayed as a Research Assistant at the Institute of Computer Vision and Robotics, INRIA. He is currently a Full Professor at the University of Salamanca in the field of photogrammetry, geodetic and cartographic engineering. He has authored more than 150 research articles in international journals and conference proceedings. Actually, he is a member of ISPRS, where he is serving as the Co-Chair for the Working Group on 'Data Acquisition and Processing in Cultural Heritage' and regularly acts as a program committee member of conferences and a reviewer for related journals. In 2015, the contribution of his works to the progress of knowledge was recognized by the Royal Academy of Engineering with the Royal Academy of Engineering Award 'Juan Lopez de Peñalver.' Based on his thesis's results, he obtained six international awards of the International Societies of Photogrammetry and Remote Sensing (ISPRS/ASPRS).